

Microwave resonances of ultrathin hexagonally symmetric microcavity arrays

J. R. Brown, A. P. Hibbins, C. R. Lawrence, M. J. Lockyear, and J. R. Sambles

Citation: *J. Appl. Phys.* **112**, 014904 (2012); doi: 10.1063/1.4729060

View online: <http://dx.doi.org/10.1063/1.4729060>

View Table of Contents: <http://jap.aip.org/resource/1/JAPIAU/v112/i1>

Published by the [American Institute of Physics](#).

Related Articles

Demonstration of nonlinear magnetoelectric coupling in metamaterials

Appl. Phys. Lett. **101**, 051103 (2012)

Silicon nanomembrane based photonic crystal waveguide array for wavelength-tunable true-time-delay lines

Appl. Phys. Lett. **101**, 051101 (2012)

Cryogenic single-shot spectroscopy of a floating poly-silicon gate transistor

J. Appl. Phys. **112**, 014510 (2012)

Microwaves in dispersive magnetic composite media (Review Article)

Low Temp. Phys. **38**, 603 (2012)

Experimental realization of a broadband conformal mapping lens for directional emission

Appl. Phys. Lett. **100**, 261907 (2012)

Additional information on J. Appl. Phys.

Journal Homepage: <http://jap.aip.org/>

Journal Information: http://jap.aip.org/about/about_the_journal

Top downloads: http://jap.aip.org/features/most_downloaded

Information for Authors: <http://jap.aip.org/authors>

ADVERTISEMENT

AIPAdvances

Special Topic Section:
PHYSICS OF CANCER

Why cancer? Why physics? [View Articles Now](#)

Microwave resonances of ultrathin hexagonally symmetric microcavity arrays

J. R. Brown,^{1,2} A. P. Hibbins,³ C. R. Lawrence,² M. J. Lockyear,³ and J. R. Sambles³

¹*Omni-ID Ltd, The Enterprise Centre, Farnham GU10 5EH, United Kingdom*

²*QinetiQ, Cody Technology Park, Farnborough GU14 0LX, United Kingdom*

³*Electromagnetic Materials Group, School of Physics, University of Exeter, Devon EX4 4QL, United Kingdom*

(Received 27 January 2012; accepted 11 May 2012; published online 9 July 2012)

A metamaterial surface formed by three slot gratings at 60° to each other has two possible high-symmetry arrangements. One forms equilateral triangular metal patches, the other a combination of hexagons and small equilateral triangles. When spaced above a ground plane with a thin dielectric spacer both structures give strong microwave absorption at certain resonant frequencies, which is largely angle independent. The results of microwave reflectivity measurements are here presented for the two distinct sample geometries and compared with predictions from finite element method models. © 2012 American Institute of Physics. [<http://dx.doi.org/10.1063/1.4729060>]

I. INTRODUCTION

Previous work^{1,2} by the current authors has concerned the characterisation of the microwave frequency-dependent reflectivity of one-dimensional microcavity arrays formed from a thin dielectric sandwiched between an upper metal layer that is perforated by a periodic array of sub-wavelength slits and a lower ground plane. The azimuthal-dependence of the microwave reflectivity response of this structure was reduced by adding a second set of slits perpendicular to the first set, thereby producing a two dimensional square array of square microcavities having 90° rotational symmetry.³

A further increase in rotational invariance might be anticipated by using three sets of slits each at 60° to the other two sets. Interestingly, there are two types of such structures with high symmetry as illustrated in Figs. 1(a) and 1(b) below. Both metamaterial surfaces have hexagonal symmetry but while one structure has only equilateral triangle metal patches, the other has hexagonal patches as well as small equilateral triangle patches. The higher order rotational symmetry of either may be expected to further improve the azimuthal independence of the resonant modes but it is not clear immediately as to what the different effects of the two distinct hexagonal geometries will be.

Hexagonal symmetry has been exploited previously by Lockyear *et al.*⁴ to reduce the azimuthal dependence of surface plasmon resonances in dual pitch metal gratings and by Suckling *et al.*⁵ to create sub-wavelength hole arrays that support azimuthally independent, surface-plasmon-mediated transmission. Sievenpiper⁶ has used hexagonally symmetric arrays of metal patches to create high-impedance ground planes that suppress the propagation of surface currents, whilst Broas^{7,8} has applied such materials to create low profile antennas for cellular phone handsets and novel phased array antennas. Others^{9,10} have used fractal configurations of triangular metal patches to create efficient absorbers of both p- (transverse magnetic, TM) and s- (transverse electric, TE) polarised radiation at microwave frequencies.

The two different hexagonal microcavity structures studied here are both shown to exhibit several highly

efficient absorption features at microwave frequencies. The azimuthal and incident angle independence of the response of some of these features is demonstrated experimentally and the results are compared to the predictions of a finite element method model.¹¹ The model is then used to explore the nature of the resonant modes excited and to elucidate the differences between the two structures.

II. EXPERIMENTAL DETAILS

The experimental co-ordinate system and sample geometries are shown in Fig. 1. The samples are formed from $t_c = 356 \mu\text{m}$ thick FR4 printed circuit board (PCB) made from laminated glass cloth infused with resin and bounded top and bottom by $t_m = 18 \mu\text{m}$ thick copper layers. The repeat period of each set of slits (the perpendicular distance between them) on both samples is $\lambda_g = 10 \text{ mm}$, each slit having a width of $w_s = 0.3 \text{ mm}$, being formed using standard print and etch techniques.¹²

The specular microwave reflectivity of each sample is measured as a function of azimuthal and polar angles using a system comprised of a matched scalar network analyser connected to reference and signal detectors, and a pair of horn antennas. The sample is placed on a turntable, the rotation of which is controlled by a stepper motor. Radiation from the transmit antenna is collimated and directed onto the sample using a spherical mirror. The polarisation state of the antennas can be varied individually, allowing for the response to p- and s-polarised radiation to be recorded. Measurements are taken at polar angles (θ) between 16° and 73° and the sample rotated between 0° and 60° azimuth (ϕ), with the full azimuthal behaviour being obtained from the rotational symmetry of the sample.

On the first trigrating sample all three sets of slits intersect at common points creating an array of equilateral triangles of side L_t given by $L_t = \sqrt{3}(2/3\lambda_g - w_s) = 11.03 \text{ mm}$ (see Fig. 1(a)). In the second structure, each set of grooves is offset by half its repeat period relative to the other two sets. Hence, all points of intersection feature slits from only two of the three sets and a pattern of hexagons of side length

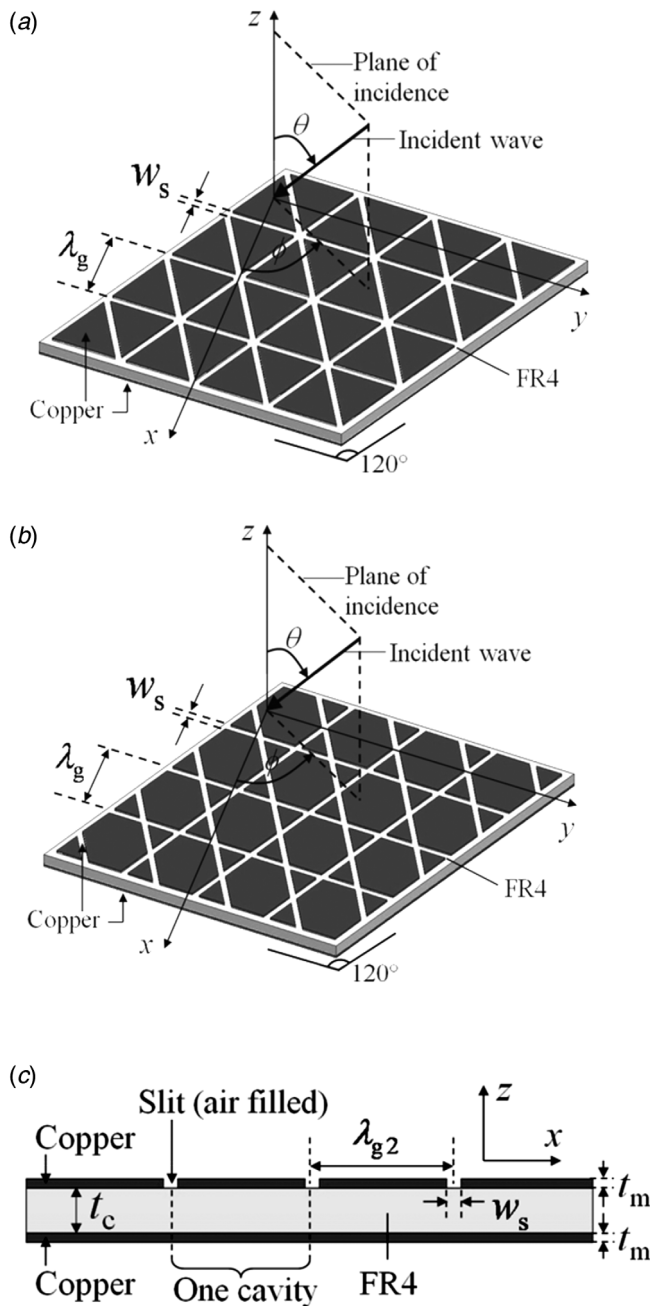


FIG. 1. The two tri-grating geometries (not to scale) and the co-ordinate system used: θ is the polar angle, ϕ is the azimuthal angle, $\lambda_g = 10$ mm, $w_s = 0.3$ mm. (a) 3-D projection of tri-grating 1. (b) 3-D projection of tri-grating 2. (c) Cross-section through the tri-grating structure, one set of slits shown for clarity, $t_m = 18 \mu\text{m}$, $t_c = 356 \mu\text{m}$, sample area is 500 mm by 500 mm.

$L_h = (1/\sqrt{3})(\lambda_g - w_s)$ interspersed with small equilateral triangles of side length $L_{st} = (1/\sqrt{3})(\lambda_g - 3w_s)$ is formed—see Fig. 1(b). For each hexagon, there are two associated small triangles. These two distinct hexagonal structures represent the two simplest hexagonally symmetric configurations. Comparison of their relative responses will help to elucidate how the size and shape of the metal patches determine the microwave response and also establish their possible use as angle-independent selective absorbers.

III. THEORY

As demonstrated for both the mono-grating structure^{1,2} and the bi-grating structures,³ these tri-gratings support TM-type waveguide modes within the dielectric layer. For the mono-grating and the bigrating, these modes resonate in a region beneath the parallel-sided metallic regions of the illuminated surface.¹³ In the present case, we do not have simple parallel sided regions but hexagonal and triangular patches. One approach to predicting the mode frequencies, particularly because, as we see later, the modes are flat banded, is to treat each of the metal patches as individual resonators. For small gaps between the patches and the ground plane the TM modes supported will have the same frequencies (ignoring edge effects) as the TE modes of the same cross section infinite waveguide. This arises because the E and B fields reverse their roles for the two situations.¹⁴ The boundary condition of a perfect conductor in a metal waveguide are here substituted with a “perfect H” boundary, while the infinitely long waveguide is substituted by a “zero” thickness capacitor. In the case of the equilateral triangle there are analytic solutions to the frequencies of the TE waveguide modes^{15,16} given by

$$f_{MN} = (c/n)(2/\sqrt{3}L_1)(M^2 + N^2/3)^{1/2}, \quad (1)$$

where M and N are integers, and n is the refractive index (~ 2.04) of the FR4 dielectric core. For sample (2) there are no analytic solutions for the hexagonal patches although there are numerical solutions for the TM waveguide modes.¹⁷ Very recently numerical solutions have also been developed for the TE waveguide modes,¹⁸ although only the lowest two modes have been quantified. These give frequencies of

$$f_p = (c/n)(2a_p)^{-1}/L_h, \quad (2)$$

where $a_1 = 1.563$ and $a_2 = 0.953$, leading to 8.5 GHz and 13.8 GHz, respectively.

The work of Bauer and Reiss,¹⁷ however, shows that the waveguide modes of the equivalent area circle are to within a few percent the same as that of the hexagon and thus we can extend these mode frequency estimates quite readily to higher orders by using the solutions of the equivalent area circles as approximations for the TE waveguide modes and hence for the TM modes under the hexagonal patches. The area of the hexagon is $1.5\sqrt{3}L_h^2$ leading to an equivalent circle radius of $r_e = (1.5\sqrt{3}/2\pi)^{1/2}L_h$. The TE resonant modes for a circular waveguide are Bessel functions with frequencies numerically evaluated using

$$f_{MN} = (c/2\pi)p'_{MN}/r_e, \quad (3)$$

where the lowest four values of p'_{MN} are 1.841 (p'_{11}), 3.054 (p'_{21}), 3.832 (p'_{01}), and 5.331 (p'_{12}). This then predicts the lowest mode frequencies for the dielectric filled cavities under the hexagonal patches of

$$f_{MN} \sim (c/n)(6\pi\sqrt{3})^{-1/2}p'_{MN}/L_h. \quad (4)$$

Comparing the numerical coefficients for the lowest two modes from Eqs. (2) and (4) we find 0.320 and 0.322 for mode 1 and 0.525 and 0.534 for mode 2. Thus, the equivalent circle approximation is satisfactory to within 2%, which will serve our purpose here.

IV. RESULTS

A. Tri-grating sample 1

The greyscale plots of Fig. 2 show the specular (a) R_{pp} and (b) R_{ss} reflected intensities from the tri-grating 1 sample, where the subscripts refer to the incident and detected polarisations, respectively. The data are shown as a function of frequency and azimuthal angle with $\theta = 16^\circ$, Figs. 2(c) and 2(d) again show R_{pp} and R_{ss} , respectively, for tri-grating sample 1 but with $\theta = 43^\circ$.

The dark bands at 8.3 GHz, 15.0 GHz, 17.3 GHz, and 17.8 GHz in Figs. 2(a) and 2(c) indicate strong absorption. These are very flat bands and suggest strongly localized modes. Treating the triangular patches as isolated resonators, Eq. (1) gives frequencies of 8.9 GHz for the (0,1) mode, 15.4 GHz for the (1,0) mode and 17.8 GHz for both the (1,1) and (0,2) modes. With experimental modes at 8.3 GHz, 15.0 GHz, 17.3 GHz, and 17.8 GHz it is clear that to explain these differences near-fields associated with the proximity of the other triangles are perturbing the mode frequencies. The data in Figs. 2(b) and 2(d) show that for R_{ss} the 15.0 GHz mode is not visible at $\theta = 16^\circ$ whilst the other three modes are still present, whereas for $\theta = 43^\circ$ a mode does appear at approximately 15.5 GHz but its strength exhibits a high degree of azimuthal dependence being optimally coupled at 30° and not being excited at 0° and 60° . It is worth noting that this is the (1,0) mode for the triangle and needs incident fields which can excite such a mode and it can be explained

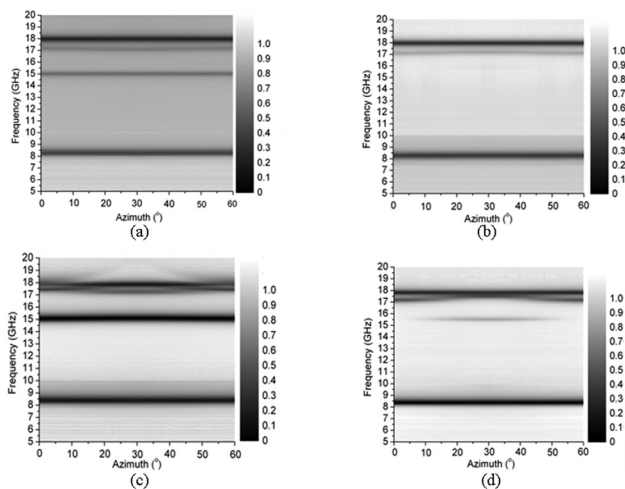


FIG. 2. Reflectivity data from tri-grating sample 1: (a) experimental R_{pp} data as a function of frequency and azimuthal angle at $\theta = 16^\circ$; (b) experimental R_{ss} data as a function of frequency and azimuthal angle at $\theta = 16^\circ$; (c) experimental R_{pp} data as a function of frequency and azimuthal angle at $\theta = 43^\circ$; (d) experimental R_{ss} data as a function of frequency and azimuthal angle at $\theta = 43^\circ$. (Note that the change of background at about 10 GHz arises from a small scaling error when the microwave horns are changed to cover different frequency bands.)

by using the finite element method model¹¹ to examine the mode's field distribution, as is shown later.

A cross-section through the greyscale plot showing R_{pp} at $\theta = 43^\circ$ and $\phi = 30^\circ$ for tri-grating 1 is shown in Fig. 3(a). The dark bands from the greyscale plots now appear as resonance dips in these line-plots. The resonances at 8.3 GHz, 15.0 GHz, and 17.8 GHz are strongly coupled and result in minimum reflectivities of less than 0.2. The mode at 17.3 GHz is less strongly coupled: Exhibiting a minimum reflectivity of ~ 0.45 , it appears to overlap the 17.8 GHz mode. These two modes should, in isolated patches with no edge effects, be at the same frequency of double the fundamental mode as they correspond to the (1,1) and (0,2) modes of the triangular waveguide. Also shown is the reflectivity as predicted by a finite element method model (solid line)¹¹ for the same incident angles. The finite element method prediction was obtained using the previously determined² values of permittivity for FR4 ($\epsilon_r = 4.17 + 0.07i$) with a period of 10 mm and slit width

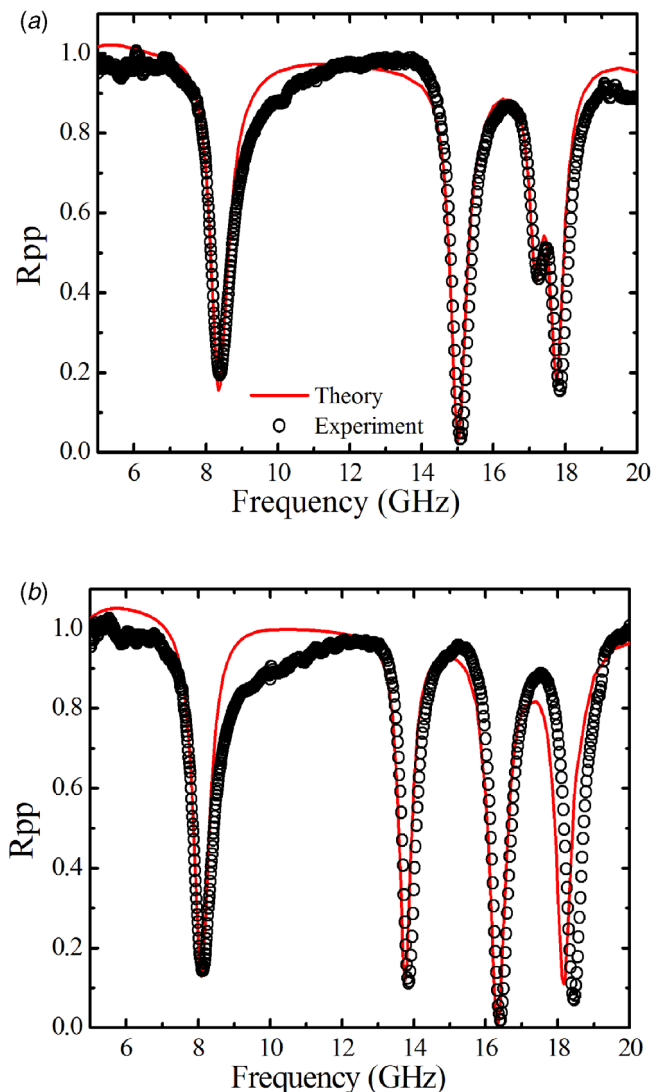


FIG. 3. Reflectivity data from tri-grating samples 1 and 2: (a) line plot showing comparison of measured data (circles) to the predictions of the numerical model (solid line) for tri-grating 1: R_{pp} $\theta = 43^\circ$, $\phi = 30^\circ$; (b) line plot showing comparison of measured data (circles) to the predictions of the numerical model (solid line) for tri-grating 2: R_{pp} $\theta = 43^\circ$, $\phi = 30^\circ$.

of 0.3 mm, and is an excellent match for the fundamental resonance: Both the depth and frequency of the resonance closely match the measured data. For the higher order modes, the model continues to accurately predict the resonant depth, but the model underestimates the resonant frequencies by approximately 0.05 GHz to 0.1 GHz.

It is important to note here that for the fundamental mode, the sample is non-diffracting over the entire range of incident angles. Hence radiative decay through propagating diffracted orders is not an available loss channel. Simulations (not included) have shown that energy dissipation via Joule heating of both the copper ground plane and patches on resonance account for less than 5% of the absorption displayed here, with the remaining power dissipated in the dielectric core. It is therefore the imaginary component of the dielectric constant (ϵ_i) of the core that dominates the shape of the reflectivity minima in the specular reflection. Fig. 4(a) shows

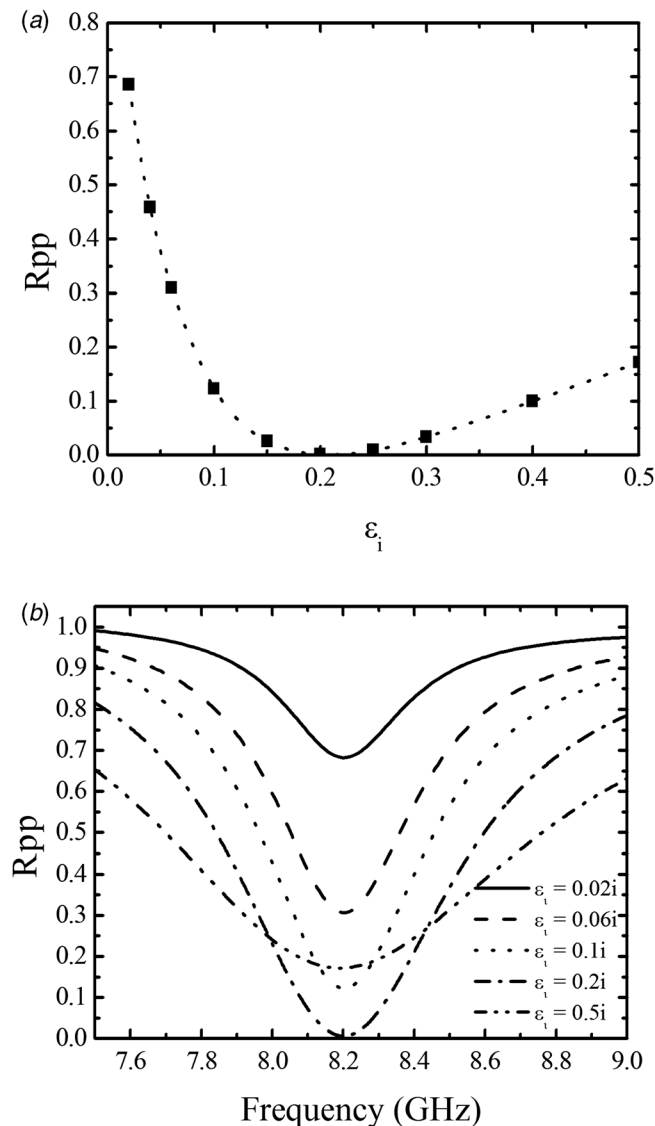


FIG. 4. Predictions from the finite element method model for tri-grating 1a at $\theta = 0^\circ$ and $\epsilon_r = 4.1$: (a) line plot showing the specular reflectivity of the fundamental mode on resonance as a function of ϵ_i , showing optimum absorption efficiency for $\epsilon = 4.1 + 0.2i$; (b) reflectivity as a function of frequency for selected values of ϵ_i , showing the deepening and then broadening of the fundamental mode with increasing ϵ_i .

the resonant reflectivity from the sample at a frequency corresponding to the fundamental mode for radiation incident at $\theta = 0^\circ$, calculated using the FEM model and plotted as a function of ϵ_i ($\epsilon_r = 4.1$). As ϵ_i is increased, the absorption goes through a maximum for $\epsilon = 4.1 + 0.2i$ and then reduces as ϵ_i continues to increase. This is due to the resonance moving from an under coupled to over coupled state through an optimum coupling condition. Inspection of Fig. 4(b) shows the resonant minimum as a function of frequency for selected values of ϵ_i , and the characteristic deepening of the resonance as the optimum coupling condition is realised. At $\epsilon_i = 0.2$ re-radiation of the mode into the specular reflection is equal in amplitude to, and in anti-phase with, the direct reflection from the sample, causing cancellation due to destructive interference. On further increase in the imaginary component, the mode shallows and broadens. The sample presented here is not optimised for absorption.

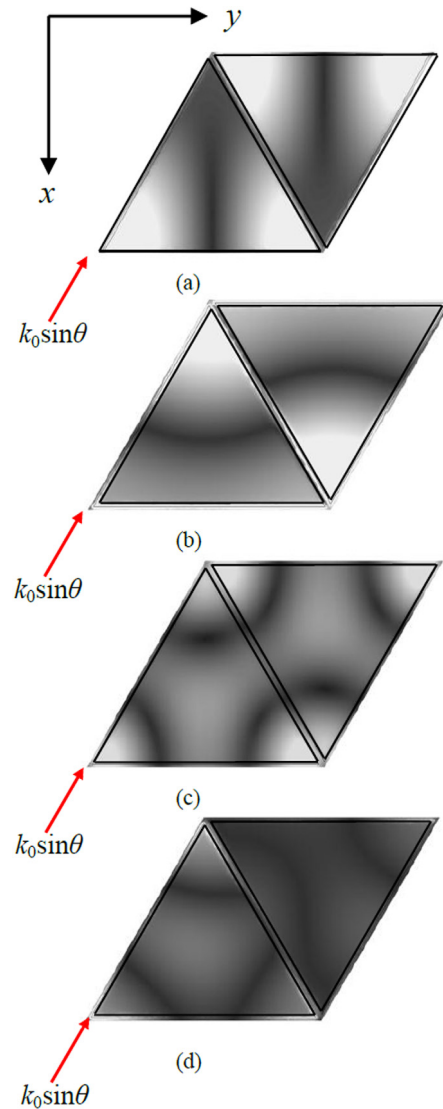


FIG. 5. Predictions of the time averaged electric field strength for tri-grating sample 1 calculated over the xy -plane midway between the ground plane and the metallic tri-grating surface for (a) an 8.35 GHz, p-polarised wave incident at $\theta = 43^\circ$, $\phi = 30^\circ$; (b) an 8.35 GHz, s-polarised wave incident at $\theta = 43^\circ$, $\phi = 30^\circ$; (c) a 15 GHz, p-polarised wave incident at $\theta = 43^\circ$, $\phi = 30^\circ$; (d) a 15 GHz, s-polarised wave incident at $\theta = 43^\circ$, $\phi = 30^\circ$. Light regions correspond to a field enhancement of 15.

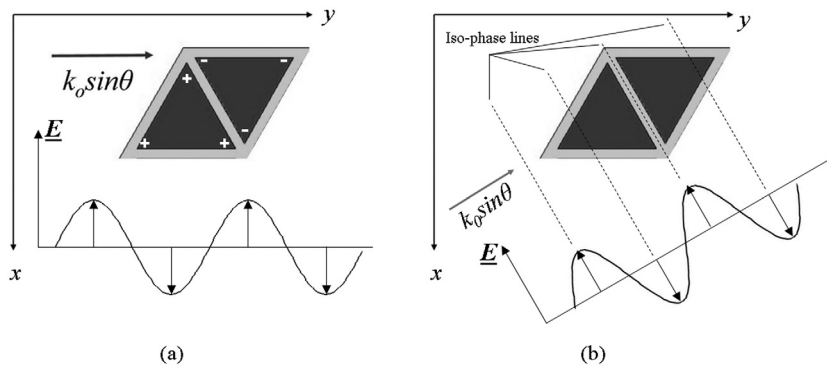


FIG. 6. Diagrams showing the incident electric field and resulting charge distribution on tri-grating sample 1 for a 15 GHz s-polarised wave incident at (a) $\phi = -90^\circ$; (b) $\phi = -60^\circ$.

The finite element method model¹¹ has been used to plot the modulus of the electric field vector calculated over the xy -plane midway between the ground plane and the metallic surface of tri-grating sample 1 at the resonant frequencies of 8.3 and 15.0 GHz for $\theta = 43^\circ$ and $\phi = 30^\circ$ in Fig. 5.

In Fig. 5(a), the incident wave has a frequency of 8.3 GHz and is p-polarised having an electric field component parallel to the y -axis; this results in a resonant mode with a field pattern that is in some measure similar to that of the half-wavelength modes supported by the bi-grating.³ This is seen by taking a line vertically through the centre of Fig. 5(a) for which E-fields will reverse along that line. However, it is also apparent that both triangular patches are exhibiting similar field distributions along their upper and lower edges, respectively. Thus, they are somewhat equivalent to a 60° lozenge with a resonance having zeros running along the x -direction at both the cell corners and the cell centres. An 8.3 GHz, s-polarised incident wave also results in a half-wave resonance, with a field distribution again determined by the direction of the electric field, which is parallel to the x -axis, see Fig. 5(b). Here it is apparent that the resonance is equivalent to the TE (0,1) mode of the equilateral triangle.

Figs. 5(c) and 5(d) show the electric field vector at 15.0 GHz for p-polarised and s-polarised waves, respectively. In both cases, resonant modes are excited in which the anti-nodes appear at and mid-way between the corners of the triangular patches. However, in neither case are the strongest fields confined to the sides of the patches that are parallel to the y -axis. In contrast to the mode at 8.3 GHz, the fields appear to be approximately equal in strength along all edges, indicating that this is the (1,0) resonant mode of the triangle.

For s-polarisation, the antinodes at the vertices of one triangle are half a cycle out of phase with those at the vertices of the other triangle (not apparent in the figure due to time averaging): The charge accumulations are of opposite sign. To couple to the 15.0 GHz mode, the electric field of the incident wave must create this charge distribution: see Fig. 6(a). However, for s-polarisation, at $\phi = -60^\circ, 0^\circ, 60^\circ$, etc. the electric field lies parallel to one of the sets of slits. In Fig. 6(b), $\phi = -60^\circ$, for example, it is parallel to the slit between the two triangles shown. The electric field of the incident s-polarised wave is in-phase everywhere along this slit; therefore, the charge accumulations at adjacent vertices of the two triangles will be the same. Upon rotation in azimuth through another 60° the electric field will be in-phase

everywhere along the next set of slits and owing to the 60° rotation symmetry of the structure this same behaviour will occur every 60° ; hence, this mode cannot be excited at $\phi = -60^\circ, 0^\circ, +60^\circ$, etc. as shown by the greyscale plot of Fig. 2(d). The formation of this charge distribution requires there to be a sufficient difference in the phase of the incident electric field across the unit cell. For small incident angles, there is insufficient phase difference; hence, the mode is strongly visible at 43° incidence but is not visible at 16° incidence.

The time averaged electric field magnitudes on resonance of the two higher order modes at 17.3 and 17.8 GHz are shown in Figs. 7(a) and 7(b). These predictions are calculated as eigenmodes of the structure and plotted over the xy plane midway between the ground plane and the metallic tri-grating surface. The energy distributions of both modes

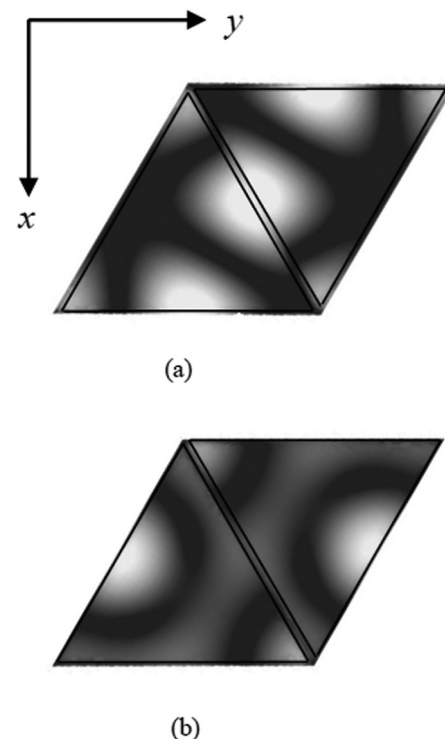


FIG. 7. Predictions of the time averaged electric field strength for tri-grating sample 1 calculated as an eigenmode solution over the xy -plane midway between the ground plane and the metallic tri-grating surface at a phase delay across the unit cell corresponding to normal incidence for (a) the 17.3 GHz and (b) the 17.8 GHz modes. Light regions correspond to regions of high field enhancement.

resemble eigen modes of the individual equilateral triangles constituting the unit cell, with the 17.3 GHz mode being associated with the (0,2) mode of the triangle and the 17.8 GHz mode associated with the (1,1). It is interesting to note that in the case of the Eigen modes of the triangle, the (0,2) and the (1,1) are degenerate, whilst here they are split by ~ 0.5 GHz due to the effect of the array. Further the (1,1) associated mode at 17.8 GHz may not be coupled to at normal incidence since symmetry arguments require a phase variance in the incident radiation across the unit cell.

B. Tri-grating sample 2

The greyscale plots of Fig. 8 show the specular (a) R_{pp} and (b) R_{ss} reflected intensities from the tri-grating 2 sample. The data are plotted as a function of frequency and azimuthal angle with $\theta = 16^\circ$. Figs. 8(c) and 8(d) again show R_{pp} and R_{ss} , respectively, for tri-grating sample 2 but with $\theta = 43^\circ$.

The dark bands at 8.1 GHz, 13.8 GHz, 16.4 GHz, and 18.3 GHz in Figs. 8(a) and 8(c) indicate strong absorption. It is worth noting immediately that the resonances are not at the same frequency as for sample 1 although the lowest order resonance is only shifted down by 0.2 GHz, and a further

resonance at 18.3 GHz is close to that at 18.1 GHz found for structure 1. The fundamental 8.1 GHz mode exhibits a high degree of azimuthal invariance, whereas the next mode (the mode at 13.8 GHz) shifts to slightly higher frequencies upon rotation towards 30° azimuth. These two modes are close in frequency to the predictions of Eq. (2) of 8.4 and 13.7 GHz, respectively. At $\theta = 43^\circ$ the highest frequency mode appears to split with two azimuthally dependent modes appearing between 17.5 GHz and 18.7 GHz.

Both the measured data and the predictions from the finite element method model¹¹ demonstrate that the fundamental mode for tri-grating 2 occurs slightly lower in frequency than that of tri-grating 1 despite both samples having identical repeat periods and material properties: see Figs. 3 and 8. This may be because, in addition to the repeat period of the slits, the off-set between the sets of slits and therefore the size and shape of the patches, also affect the resonant frequencies through near field diffractive effects.

The data in Figs. 8(b) and 8(d) show that for R_{ss} the 16.4 GHz mode is not excited for either $\theta = 16^\circ$ or $\theta = 43^\circ$, this can again be explained by considering the field distribution of the mode. The other three modes are still present and occur at 8.1 GHz, 13.8 GHz, and 18.3 GHz as for p-polarisation. The

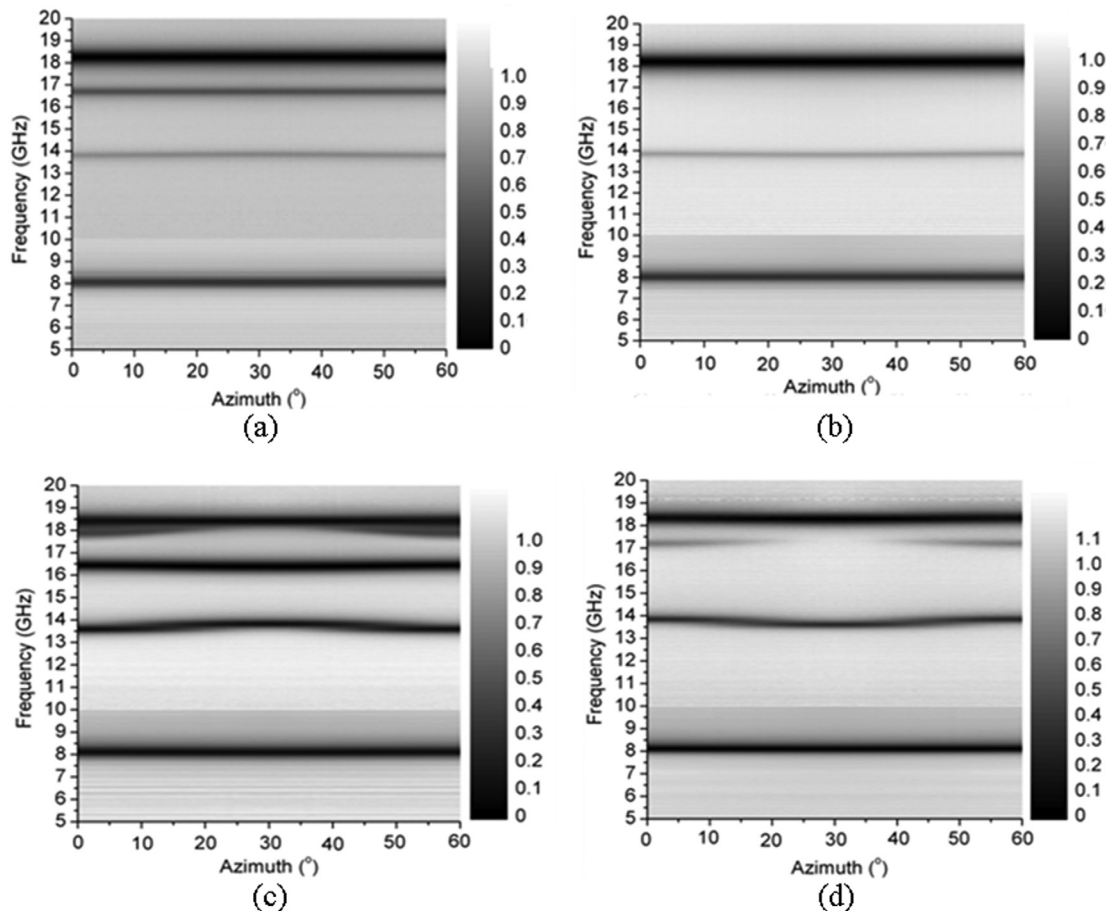


FIG. 8. Reflectivity data from tri-grating sample 2: (a) experimental R_{pp} data as a function of frequency and azimuthal angle at $\theta = 16^\circ$; (b) experimental R_{ss} data as a function of frequency and azimuthal angle at $\theta = 16^\circ$; (c) experimental R_{pp} data as a function of frequency and azimuthal angle at $\theta = 43^\circ$; (d) experimental R_{ss} data as a function of frequency and azimuthal angle at $\theta = 43^\circ$. (Note that the change of background at about 10 GHz arises from a small scaling error when the microwave horns are changed to cover different frequency bands.)

fundamental demonstrates azimuthal invariance, whereas the second harmonic mode exhibits behaviour similar to that for p-polarisation, except that it shifts down in frequency rather than up upon rotation towards 30° azimuth. Another mode appears at 17.2 GHz and is highly sensitive to azimuth, being optimally coupled at 0° and 60° azimuth, and not being excited at 30° azimuth, where the symmetry inhibits coupling for close to normal incidence. The 18.3 GHz mode remains largely stable in frequency with only a minor shift down upon rotation to 30° azimuth.

A cross-section through the greyscale plot showing R_{pp} at $\theta = 43^\circ$ and $\phi = 30^\circ$ for tri-grating 2 is shown in Fig. 3(b). The dark bands from the greyscale plots appear as resonances in this cross-section. All four resonances are strongly coupled and result in minimum reflectivities of less than 0.2. Also shown is the reflectivity as predicted by a finite element method model¹¹ for the same incident angles. The model predicts the frequency and depth of the fundamental resonance very accurately: For the higher order modes, the model continues to accurately predict the resonant depth, but there is a slight disagreement in frequency, with the model underestimating the resonant frequencies by approximately 0.05 GHz to 0.2 GHz.

The finite element method model¹¹ can be used to examine the field distribution of the modes shown in Figs. 3 and 8: It has been used to plot the time-averaged electric field strength over the xy -plane midway between the ground plane and tri-grating surface at the resonant frequencies of 8.1 and 13.8 GHz for $\theta = 43^\circ$ and $\phi = -60^\circ$ in Fig. 9. In Fig. 9(a), the incident wave has a frequency of 8.1 GHz and is p-polarised: The region beneath the central hexagon supports a half-wave resonant mode. An 8.1 GHz s-polarised radiation incident at the same angle also excites a half-wave mode beneath the hexagonal patch, although the mode appears transverse to the plane of incidence due to the polarisation of the incident wave, see Fig. 9(b). This would seem to be the fundamental mode of a hexagonal plate. The equivalent area circle fundamental mode, using Eq. (5) is expected to be at 8.45 GHz, with the next two modes at 14.2 GHz and 17.6 GHz. These modes are all somewhat higher in frequency than observed but near-field diffraction due to edge effects and the proximity of other metal patches may well cause this.

Figs. 9(c) and 9(d) show the electric field vector at 13.8 GHz for waves p-polarised and s-polarised, respectively: Both polarisations excite modes in which there are field anti-nodes on opposing sides of the central hexagon which are in-phase with each other. Half-wavelength modes would exhibit antinodes that were half a cycle out of phase with each other, and wavelength modes would require an additional anti-node in the centre of the hexagon. This corresponds to the mode symmetry of the (2,1) resonant hexagonal “waveguide” mode, expected at around 14.2 GHz.

Shown in Fig. 10(a) is a plot of the time averaged electric field strength for a 16.4 GHz p-polarised wave incident at $\theta = 43^\circ$, $\phi = -60^\circ$. The fields are again confined to the region beneath the hexagon and exhibit a one-wavelength resonance: The anti-node at the centre of the hexagon is half a cycle out of phase with that which appears around the pe-

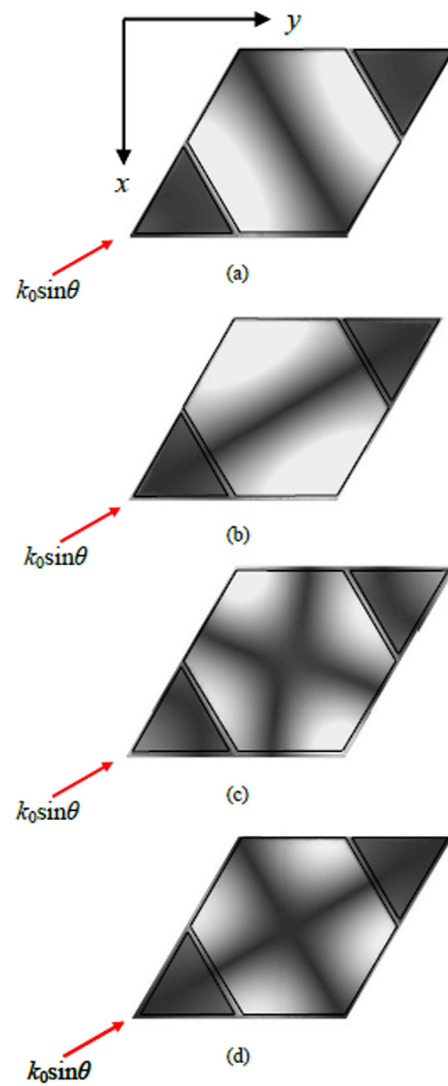


FIG. 9. Predictions of the time-averaged electric field strength for tri-grating sample 2 calculated over the xy -plane midway between the ground plane and the metallic tri-grating surface for (a) an 8.1 GHz, p-polarised wave incident at $\theta = 43^\circ$, $\phi = -60^\circ$; (b) a 8.1 GHz, s-polarised wave incident at $\theta = 43^\circ$, $\phi = -60^\circ$; (c) an 13.8 GHz, p-polarised wave incident at $\theta = 43^\circ$, $\phi = -60^\circ$; (d) a 13.8 GHz, s-polarised wave incident at $\theta = 43^\circ$, $\phi = -60^\circ$. Light regions correspond to a field enhancement of 15.

rimeter. This is the anticipated (0,1) mode with its frequency somewhat lower, at 16.4 GHz, than the estimated 17.6 GHz.

The excitation of this mode for p-polarisation is possible as the phase change across the patches causes a reversal of the direction of the electric field and the resulting components of the electric field drive charges of like sign towards the centre of the hexagon; see Fig. 10(b). However, it is not possible to create this charge distribution with s-polarisation at any azimuth because the components of the electric field do not drive like charges towards the centre, see Fig. 10(c).

The next mode up for the resonant hexagonal plate should be at 24.5 GHz (1,2) which is far higher than the well coupled mode found at about 18.3 GHz. However, the (0,1) mode of the small equilateral triangular plates, which is calculated from Eq. (2) using a side length of 5.3 mm, is 18.7 GHz and this fits well with the frequency recorded.

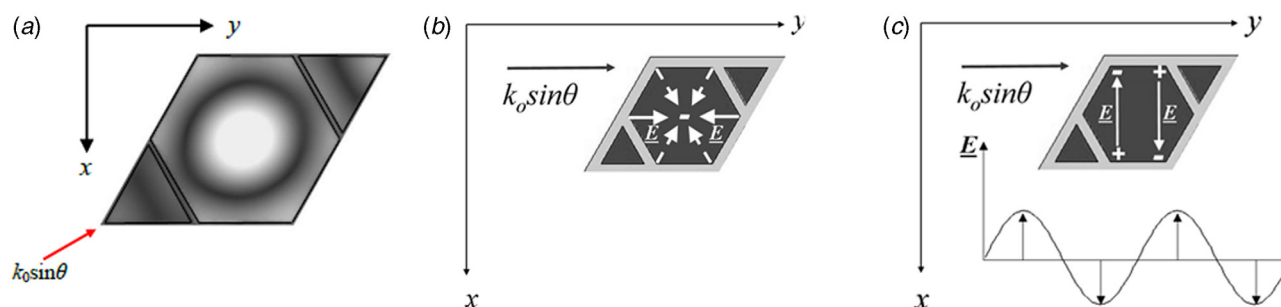


FIG. 10. For tri-grating sample 2: (a) prediction of the time averaged electric field strength calculated over the xy -plane midway between the ground plane and the metallic tri-grating surface for (a) 16.4 GHz, p-polarised wave incident at $\theta = 43^\circ$, $\phi = -60^\circ$; (b) diagram showing the incident electric field and resulting charge distribution for a p-polarised wave incident at $\phi = -90^\circ$; (c) diagram showing the incident electric field and resulting charge distribution for a s-polarised wave incident at $\phi = -90^\circ$.

Thus in tri-grating sample 2, there are two distinct types of localised resonances: those associated with the large hexagon and those associated with the small equilateral triangle. Interestingly, while the spatial occupancy of hexagons and triangles is of necessity less than 100% the coupling efficiency to all the primary modes is of order 90%. This is particularly noteworthy for the fundamental mode of the small triangle since the actual percentage area occupied by these triangles is less than 25%.

V. CONCLUSIONS

It has been demonstrated by both theory and experimental measurement that microcavity arrays with hexagonal symmetry can be tailored to produce highly efficient microwave absorption that is independent of azimuthal and incident angle. The two hexagonally symmetric structures studied herein support a series of resonant modes for both p-polarised and s-polarised incident radiations, the frequencies approximately predicted by considering the resonant modes underneath individual metal patches. For the second sample type containing both hexagonal patches and equilateral triangles resonances from both types of patch are found, both resonances being nearly 100% deep even though the occupancy for each type of patch is much less than 100%.

These thin microcavity absorbing structures could be applied to reduce the level of backscattered radiation in environments where the direction and polarisation of incident radiation are varying or unpredictable. Examples of such environments include: airports where reflections from buildings can cause significant interference problems; and the interior of buildings where screening from electromagnetic radiation is required. Furthermore, the thin, flexible and lightweight nature of the material makes it ideal for

electromagnetic compatibility (EMC) applications where space is critical such as on or within the housing of sensitive instruments.

ACKNOWLEDGMENTS

The authors would like to acknowledge funding from the EPSRC, Omni-ID, and QinetQ Ltd.

- ¹A. P. Hibbins, W. A. Murray, J. Tyler, S. Wedge, W. L. Barnes, and J. R. Sambles, *Phys. Rev. B* **74**, 073408 (2006).
- ²A. P. Hibbins, J. R. Sambles, C. R. Lawrence, and J. R. Brown, *Phys. Rev. Lett.* **92**, 143904 (2004).
- ³J. R. Brown, A. P. Hibbins, M. J. Lockyear, C. R. Lawrence, and J. R. Sambles, *J. Appl. Phys.* **104**, 043105 (2008).
- ⁴M. J. Lockyear, A. P. Hibbins, J. R. Sambles, and C. R. Lawrence, *Appl. Phys. Lett.* **86**, 184109 (2005).
- ⁵J. R. Suckling, J. R. Sambles, and C. R. Lawrence, *New J. Phys.* **9**, 1 (2007).
- ⁶D. Sievenpiper, L. Zhang, R. F. J. Broas, N. G. Alexopolous, and E. Yablonovitch, *IEEE Trans. Microwave Theory Tech.* **47**, 2059 (1999).
- ⁷R. F. J. Broas, D. Sievenpiper, and E. Yablonovitch, *IEEE Trans. Microwave Theory Tech.* **49**, 1262 (2001).
- ⁸R. F. J. Broas, D. Sievenpiper, and E. Yablonovitch, *IEEE Trans. Antennas Propag.* **53**, 1377 (2005).
- ⁹A. R. Chandran, T. Matthew, T. K. Aanandan, P. Mohanan, and K. Vasudevan, *Electron. Lett.* **40**, 1245 (2004).
- ¹⁰A. R. Chandran, T. Matthew, T. K. Aanandan, P. Mohanan, and K. Vasudevan, *Microwave Opt. Technol. Lett.* **40**, 246 (2004).
- ¹¹*High Frequency Structure Simulator* (Ansoft, Pittsburgh, PA, USA).
- ¹²Eurotech Group plc., Exmouth, UK.
- ¹³Y. Takakura, *Phys. Rev. Lett.* **86**, 5601 (2001).
- ¹⁴M. J. Lockyear, A. P. Hibbins, J. R. Sambles, P. A. Hobson, and C. R. Lawrence, *Appl. Phys. Lett.* **94**, 04191326 (2009).
- ¹⁵M. A. Pinsky, *SIAM J. Math. Anal.* **11**, 819 (1980).
- ¹⁶P. L. Overfelt and D. J. White, *IEEE Trans. Microwave Theory Tech.* **34**, 161 (1986).
- ¹⁷L. Bauer and E. L. Reiss, *SIAM J. Appl. Math.* **35**, 508 (1978).
- ¹⁸V. V. Komarov, *J. Infrared Millim. Terahertz Waves* **32**, 40 (2011).